

Response of Cr and Cr-Al coatings on Zircaloy-2 to high temperature steam



Weicheng Zhong, Peter A. Mouche, Brent J. Heuser*

Department of Nuclear, Plasma, and Radiological Engineering, University of Illinois, Urbana, IL 61801, USA

HIGHLIGHTS

- The oxidation behavior of Cr and CrAl coatings on Zircaloy-2 has been characterized in high temperature steam.
- CrAl coatings demonstrated three orders magnitude lower weight gain than uncoated Zircaloy-2 in 700 °C steam environment.
- CrAl coatings with higher Al composition demonstrated lower weight gain in high temperature steam.
- Dissolution of second phase particles occurs on the coated Zircaloy-2 during the high temperature steam exposure.

ARTICLE INFO

Article history:

Received 6 July 2017

Received in revised form

12 September 2017

Accepted 8 October 2017

Available online 9 October 2017

Keywords:

Zircaloy

Oxidation

Chromium coating

Chromium-aluminum coatings

Second phase particle

ABSTRACT

The oxidation behavior of chromium (Cr) and chromium-aluminum (CrAl) coatings with various compositions deposited on Zircaloy-2 to 700 °C high-temperature steam (HTS) exposure has been investigated. CrAl coatings with higher Al compositions demonstrate lower oxidation weight gain. A layer of γ -alumina developed on the CrAl coatings with Al composition over 43 at%, while Al_2O_3 and Cr_2O_3 developed on CrAl coatings with Al composition below 33 at%. Oxidation of Zircaloy-2 substrate was inhibited by the 1 μm coatings to 20 h HTS exposure. Coating constituent elements diffused into the substrate and formed intermetallic phases with the Zircaloy substrate. Thicker layers of intermetallic phases developed on the coatings with higher Al composition. The intermetallic phases included Fe and Ni, indicating the dissolution of second phase particles (SPPs) during HTS exposure.

© 2017 Elsevier B.V. All rights reserved.

1. Introduction

The Fukushima accident highlighted potential issues associated with current LWR fuel, including accelerated hydrogen production rate, rapid oxidation in elevated temperatures, and significant heat production from oxidation during high-temperature steam (HTS) exposure associated with off-normal transients. All of these issues are detrimental to the ductility of cladding, and lead to the potential loss of cladding as a barrier. Our works aim to mitigate the oxidation of Zircaloy-2 via Cr and CrAl coatings, and demonstrate the response of the coatings on Zircaloy-2 to HTS exposure.

There are currently three main strategies to improve the accident tolerant properties for cladding materials [1,2], 1) modification of compositions and/or processing of the Zirconium-based alloys [3,4], 2) development of non-Zircaloy monolithic alternative

materials [5–13], and 3) application of coatings to Zircaloy cladding [14–22].

Reduced oxidation rate and hydrogen uptake were observed for the advanced Zirconium-based alloys, such as M5, ZIRLO, and E110, etc. [3,4]. However, improvement by minor composition changes is expected to be limited, especially at elevated temperatures [23,24]. Alternatives to non-Zircaloy materials, such as iron-chromium-aluminum (FeCrAl) alloy [5–8] and Silicon Carbide (SiC) ceramics [9–13] demonstrate promising mechanical and oxidation properties. More research for the compatibility in LWRs is on-going. The third strategy is to apply an oxidation resistant coating to Zircaloy cladding. Multiple coating systems have been studied by different groups, which can be categorized into ceramic coatings and metallic coatings. Ceramics coatings, such as SiC [16,17] and MAX phases [18,19], demonstrate better corrosion and oxidation properties than Zircaloy. Metallic coating, especially Cr, demonstrates superior oxidation resistant and maintains integrity in accident scenarios with good adhesion [20–22]. FeCrAl coatings have been

* Corresponding author.

E-mail address: bheuser@illinois.edu (B.J. Heuser).

studied in both high temperature and simulated BWR environment [14,15,21]. However, the eutectic reaction of Fe-Zr near 900 °C induces complete coating loss above this temperature.

Most published work regarding coatings demonstrated better oxidation and corrosion behavior, and good adhesion with the substrate. However, little work has discussed the coating-substrate interaction. Although the interaction of coating and substrate is expected to improve the adhesion of coatings, it can potentially consume thin coatings, which would reduce the effectiveness of this solution pathway [25].

In this study, CrAl and Cr coatings have been deposited on Zircaloy-2 and the oxidation behavior during 700 °C HTS exposure has been characterized. Micro-analytical techniques have been applied to investigate the microstructure of as-grown and post-exposure coatings. Crystal lattice structure and composition of exposure products will be presented in Section 3 using X-ray diffraction (XRD) and (scanning) transmission electron microscopy (STEM) with the capability of energy dispersive spectroscopy (EDS). Discussion regarding the protection of coatings with different compositions, and the interaction between the coatings and the substrate will be presented in Section 4, followed by conclusions.

2. Experimental approach

2.1. CrAl and Cr coating deposition

CrAl and Cr coatings were deposited on polished Zircaloy-2 using a dedicated magnetron sputtering system [14,26]. Zircaloy-2 plates were provided by ATI Specialty Alloys and Compounds. Pure Cr and pure Al targets were used for the deposition and the compositions of coatings were controlled by the power to the two sputtering targets. The base pressure of the system was on the order of 10^{-8} Torr. Polished Zircaloy-2 coupons were pre-heated to 350 °C for 2 h before the deposition, and the deposition was performed at 200 °C. Argon was introduced into the chamber at a flow rate of 3 sccm with a working pressure of 1mTorr. The typical deposition rate was 8 nm/min, and the deposition of 1 μm coatings was completed in about 2 h. The deposition rates were calibrated by the examination of coatings on Si wafers in cross section with a scanning electron microscope. Table 1 is the matrix of the samples used in this study with the coating composition and thickness. Cr and CrAl coatings with four different composition (Cr/Al atomic percent of 42/58, 57/43, 67/33, and 81/19) were studied.

2.2. Thermogravimetric analysis

Coatings were deposited on both sides of $10 \times 10 \times 1$ mm³ polished Zircaloy-2 coupons. Four edges of the sheets received partial or no coating during the deposition. Coated Zircaloy samples were exposed to 700 °C HTS in a commercial NETZSCH Jupiter 441 Simultaneous Thermal Analyzer (STA) with a steam generator. The description of the STA was provided in the previous work [14]. Oxidation of the uncoated/partially coated Zircaloy substrate edges

is expected. Therefore, the microanalysis was performed at the center of the coated surface to avoid any edge effects.

2.3. Analytical technique

As-deposited and post-HTS-exposure Cr and CrAl coatings were characterized using scanning electron microscopy (SEM), XRD, and (S)TEM with the EDS capability. Coating compositions were determined by the plan view SEM/EDS. As-deposited and post-HTS-exposure coating morphology were examined by SEM. XRD was applied to identify sample crystal structure with glancing incident geometry to minimize the diffraction from the Zircaloy substrate. Focused Ion Beam (FIB) was used to prepare (S)TEM cross sectional samples. To protect the surface oxide, layers of electron beam Pt and ion beam Pt were deposited before the milling. For some samples, a 20 nm Au-Pd layer was deposited on the surface before the Pt deposition to prevent charge buildup. Cross sectional (S) TEM/EDS analysis was performed to study the microstructure and the composition of post-HTS-exposure coatings. Select area diffraction (SAD) in TEM was applied to identify the crystal structure of the thin alumina layer.

A HITACHI S-4700 high resolution SEM was used in this study. The electron source is a cold field emission gun, with 1.5 nm resolution at 15 kV. An attached Oxford Instruments ISIS EDS X-ray microanalysis system was used for composition analysis. Both a JEOL 2010F STEM and a JEOL 2010LaB6 TEM were used to study the cross section microstructure. The STEM uses a Schottky field emitter at 200 kV, with resolution of 0.18 nm. The system is capable of EDS using an Oxford INCA 30 mm ATW detector for chemical composition analysis. The TEM operates at 200 kV with the optimal point resolution of 0.28 nm. The smallest select area aperture for the TEM is about 200 nm. A Panalytical Philips X'pert MRD instrument was used to characterize the crystal lattice structures of coatings and substrate using Cu-K α beam. To emphasize the diffraction intensity from the coating, XRD was performed with a glancing incident angle of 2° for the as-deposited coated Zircaloy, and with a glancing incident angle of 3° for the post-HTS-exposure coated Zircaloy.

3. Results and analysis

3.1. XRD analysis of the as-deposited and post-HTS-exposure Cr and CrAl coatings

Glancing incident X-ray diffraction (GIXRD) on the as-deposited CrAl and Cr coatings is shown in Fig. 1A. Three phases of as-deposited coatings were indexed: Cubic Cr with the space group of Im-3m for pure Cr coating, tetragonal AlCr₂ with the space group of P4/mmm for the 67/33 CrAl coating, and rhombohedral Al₈Cr₅ with the space group of R3m for the 42/58 CrAl coating. It is noted that 81/19 CrAl coating does not have the stoichiometry of either pure Cr or AlCr₂, and the diffraction peaks lie between the cubic Cr pattern and the tetragonal AlCr₂ pattern, whose major peaks are neighboring. The 81/19 CrAl coating is also indexed as the cubic Cr phase due to a missing peak at 48°, which corresponds to the (112) peak of tetragonal AlCr₂ phase. However, we acknowledged that a mixture of cubic Cr phase and tetragonal AlCr₂ phase in the 81/19 CrAl coating cannot be ruled out due to the low intensity of the AlCr₂ (112) peak and the possibility of the texture in the coating. Similarly, for the 57/43 CrAl coating where the tetragonal AlCr₂ phase is indexed, the coexistence of both the rhombohedral Al₈Cr₅ and the tetragonal AlCr₂ phases cannot be ruled out. In addition, 81/19 CrAl and 57/43 CrAl coatings show shifted peaks position. There are two potential reasons for the peak shift: the low coating deposition temperature [27] and off-stoichiometry of the coating

Table 1
Steam exposure sample matrix showing coating compositions and thickness.

Coating	Sample ID	Composition [Cr/Al in atomic percentage]	Thickness [μm]
CrAl	42/58 CrAl	42/58	1
	57/43 CrAl	57/43	1
	67/33 CrAl	67/33	1
	81/19 CrAl	81/19	1
Cr	Cr	100/0	1

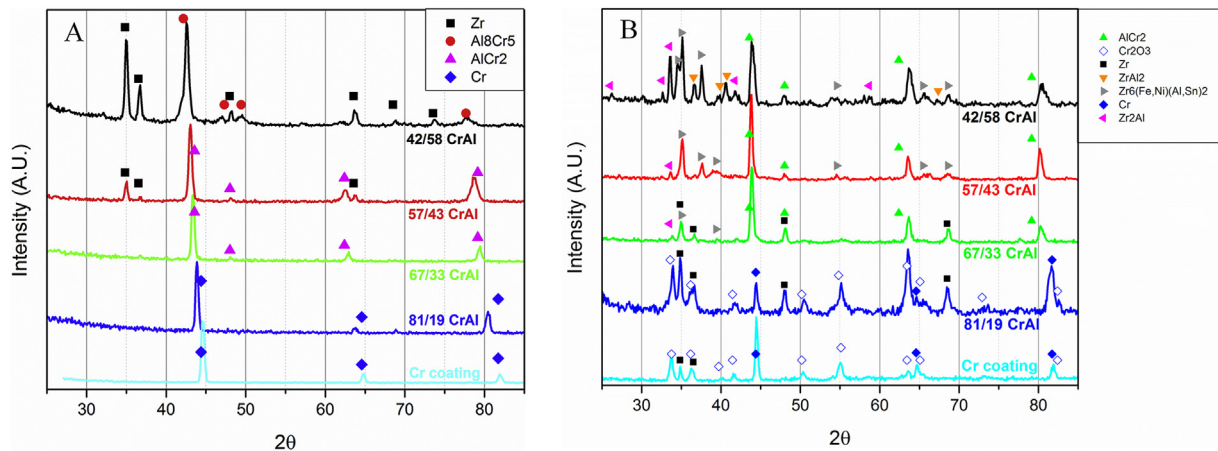


Fig. 1. Glancing incident X-ray diffraction for CrAl and Cr coatings. A) GIXRD of the as-deposited coatings at a glancing angle of 2°. B) GIXRD of the coatings after 20 h exposure to 700 °C HTS at a glancing angle of 3°. Coatings and intermetallic phases and Cr₂O₃ were indexed. The surface oxide on 57/43 CrAl, and 42/58 CrAl were too thin to be indexed. However, the crystal lattice structure of alumina on 57/43 CrAl coating was identified by SAD in TEM in Fig. 4B.

composition.

The thickness for all coatings in this study are 1 μm, but diffraction peaks from the Zr substrate were observed only for the coatings with high Al composition (42/58 CrAl and 57/43 CrAl). This is attributed to the lower mass attenuation of Al compared to Cr for Cu Kα X-rays; thus, the X-ray penetration depth is larger for higher Al composition coatings. Penetration distances of Cu Kα X-ray in the coatings were calculated using Equation (1), where μ is the mass attenuation coefficient, and I_0 and I are the incident and diffracted intensity. The linear attenuation coefficients of Cr and Al are obtained from the NIST database [28]. The density of coatings are assumed to be the theoretical density of the coating alloys, acknowledging that different coating density might be produced from the sputtering process. The penetration depth estimation uses a geometry of 2° incident angle and 35° diffraction angle, where the α -Zr (0002) peak is. Table 2 summarizes the mass attenuation coefficient and penetration depth of 95% attenuation in each coatings. The X-ray penetration depth in higher Al composition coating is larger. Although the penetration depth in 57/43 CrAl coating is less than 1 μm, the diffraction intensity of α -Zr phase was observed from the XRD measurement (Fig. 1A). This could be attributed to the over-estimated coating density and the under-estimated attenuation percentage in the penetration depth calculation.

$$L = \frac{1}{\mu} \ln\left(\frac{I_0}{I}\right) \quad (1)$$

The GIXRD results for Cr coating and CrAl coatings after 20 h exposure to 700 °C HTS are shown in Fig. 1B. Strong Cr₂O₃ peaks were observed on both Cr and 81/19 CrAl coatings. Metallic Cr peaks were also observed in the post-exposure patterns, which suggests that the coatings would provide longer protection over 20 h. There is some small diffraction intensity not indexed on the

post-HTS-exposure 81/19 CrAl and Cr coatings, which could be caused by the formation of intermetallic phases involving the coating and the substrate.

Strong peak intensity of intermetallic phases was observed for CrAl coatings with high Al composition, especially 42/58 CrAl and 57/43 CrAl coatings. Hexagonal Zr₆(Fe,Ni)(Al,Sn)₂ structure with the space group of P-62 m and hexagonal Zr₂Al structure with the space group of P63/mmc were indexed on the post-HTS-exposure CrAl coatings with the composition of 42/58 and 57/43. The peak intensities are stronger for the coatings with higher Al composition, which indicates that larger volume of intermetallic phases developed in the higher Al composition coatings. In addition, the hexagonal ZrAl₂ structure with the space group of P63/mmc was indexed on the 42/58 CrAl coating. The intermetallic phase ZrAl₂ has higher Al stoichiometry than the other two intermetallic phases, and was only observed on the coating with the highest Al composition (42/58 CrAl).

The post-HTS-exposure coatings were indexed as the tetragonal AlCr₂ (P4/mmm) for 42/58 CrAl, 57/43 CrAl, and 67/33 CrAl coatings. It is noted that the diffracted peaks are slightly shifted to higher angles. This may result from the off-stoichiometric composition in the post-HTS-exposure coatings. Phase transformation of 42/58 CrAl coating occurred after HTS exposure. Aluminum transport to the surface oxide and to the Zircaloy-2 substrate depletes Al inventory in the coating. As a consequence, the lattice structure of 42/58 CrAl coating changed from the as-deposited rhombohedral Al₈Cr₅ (R3m) structure to the post-HTS-exposure tetragonal AlCr₂ (P4/mmm) structure. The phase transformation is evident by the presence of the (200) peak of tetragonal AlCr₂ at 64°. (see Fig. 1B). Alumina layer developed on all CrAl coatings at 700 °C HTS exposure, which will be demonstrated later in the cross sectional STEM analysis. However, diffraction peaks of alumina were not indexed in the diffraction patterns because the layer is too thin to have observable peak intensity.

Table 2
Penetration depth of Cu Kα X-rays in Cr and CrAl coatings.

Coatings	Mass attenuation coefficient (cm ² /g)	Density (g/cm ³)	95% attenuation distance (μm)	Penetration depth (μm)
42/58 CrAl	167.4	4.242	42.2	1.38
57/43 CrAl	194.7	5.569	27.6	0.91
67/33 CrAl	210.4	5.569	25.6	0.84
81/19 CrAl	229.5	7.2	18.1	0.59
Cr	251.3	7.2	16.6	0.54

3.2. Cross sectional analysis by (S)TEM/EDS and surface topography by SEM

Cross sectional (S)TEM/EDS analysis was performed on the as-deposited and post-HTS-exposure CrAl coatings. Fig. 2A shows the TEM cross sectional image of the as-deposited 42/58 CrAl coating on Zircaloy-2. A columnar structure with a thickness of 1 μm is observed. CrAl grains are smaller at the coating/substrate

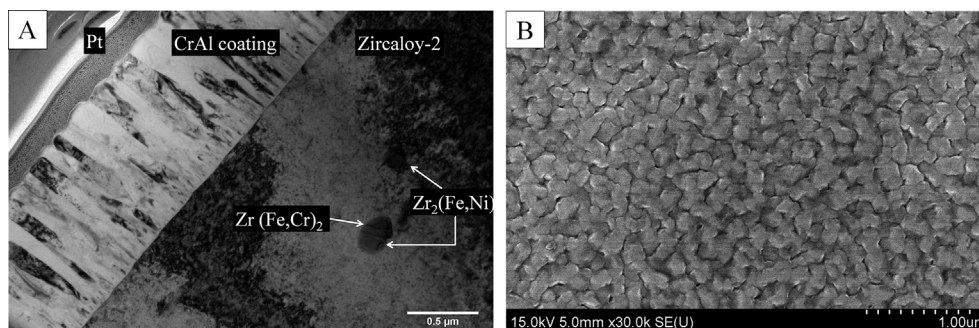


Fig. 2. Cross section and plan view images of as-deposited 42/58 CrAl coating on Zircaloy-2. A) Cross sectional TEM image of as-grown 42/58 CrAl coating on Zircaloy-2. Columnar structure of as-grown CrAl coating is observed. Three second phase particles are observed in the Zircaloy-2 matrix. B) Plan view SEM image of coating. Grain size at the surface of the coating is about 100 nm.

interface, and they grow as the coating thickens. The average grain size is approximately 100 nm at the free surface, which is also shown in the SEM plan view image in Fig. 2B. Three second phase particles (SPPs) are observed in the cross sectional STEM image with compositions corresponding to $Zr_2(Fe,Ni)$ and $Zr(Fe,Cr)_2$.

Cross sectional STEM analysis of the post-HTS-exposure CrAl coated Zircaloy-2 is shown in Figs. 3–6. Fig. 3 is the cross sectional STEM image and EDS mapping of 42/58 CrAl coating after 700 °C HTS exposure for 10 h. The vertical strips in the image are artifacts from ion beam milling during the sample preparation. Compositional EDS mapping was performed and the scanning area is labeled in the STEM image. A layer of alumina formed at the surface with a thickness of 50 nm. Layers of intermetallic phases developed below the coating and the chemical composition was measured by EDS. The composition and the thickness of each intermetallic layer are summarized in Table 3. The first intermetallic layer to form directly below the coating has the stoichiometry of $Zr(Al,Cr,Fe,Ni)_2$, where Al concentration is as high as 51 at%. This layer corresponds to the hexagonal $ZrAl_2$ phase, as indexed in GIXRD measurement in Fig. 1B. The $ZrAl_2$ intermetallic phase has high Al stoichiometry and is only observed in the high Al composition coating (42/58 CrAl), consistent with the XRD analysis (see Fig. 1B). The next layer below the hexagonal $ZrAl_2$ phase has a stoichiometry of Zr_2Al with a hexagonal structure as indexed in the GIXRD measurement. In contrast to the $ZrAl_2$ phase, the concentration of Cr, Fe and Ni is negligible in Zr_2Al phase. Finally an intermetallic phase with the stoichiometry of $Zr_2(Al,Sn,Fe,Ni)$ is observed between the Zr_2Al layer and the Zircaloy-2 substrate. The total concentration of Al and Sn in this layer is 21 at% and the total concentration of Fe and Ni is 13 at%, which are approximately equivalent to two out of nine and one out of nine respectively. This stoichiometry corresponds to the hexagonal $Zr_6(Fe,Ni)(Al,Sn)_2$ phase as observed with GIXRD. Furthermore, the $Zr_6(Fe,Ni)(Al,Sn)_2$ layer is the thickest of the three intermetallic layers, which is in agreement with the XRD peak intensity in Fig. 1B.

Iron, Ni, and Sn are observed in the intermetallic phases that formed on Zircaloy-2 during HTS exposure. However, these elements are not the constituents of the deposited coatings. Therefore, these elements must come from the Zircaloy matrix. Iron and Ni have limited solubility in Zircaloy, and are primarily contained in Zircaloy-2 as $Zr_2(Fe,Ni)$ or $Zr(Fe,Cr)_2$ SPPs [29]. The formation of intermetallic phases involving Fe and Ni suggests the dissolution of secondary phase particles during the steam exposure, which will be discussed in Section 4.4.

The presence of oxygen within the coating was observed from the EDS mapping in all post-HTS-exposure CrAl coatings, as shown in Figs. 3, 5 and 6. However, the oxygen intensity in the coatings could be an artifact from the overlap of the Oxygen $K\alpha$ peak and Cr

$L\alpha$ peak in the EDS spectrum. In addition, oxygen intensity was also observed in the as-deposited CrAl coating using STEM/EDS due to the peak overlap [not shown]. This reinforces the statement that the oxygen intensity in the coating is the artifact from the Cr peak overlap.

The coating thickness reduced to 700 nm after the HTS exposure from the as-deposited 1 μ m thickness, and all of the post-HTS-exposure CrAl coatings demonstrated porous structures, as shown in Figs. 3–6. For 42/58 CrAl and 57/43 CrAl coatings, these pores exist either at the alumina/coating interface or at the coating/intermetallic phase interface, as shown in Figs. 3 and 4. The porosity at the alumina/coating interface is attributed to the outward growth of the alumina layer and the Al needed for this growth. Outward Al diffusion from the coating must be accompanied by a counter flow of vacancies across the alumina/coating interface (the Kirkendall effect). Vacancies accumulated at the interface and lead to pore formation. This also explains the pore formation at the coating/intermetallic phase interface, where vacancy accumulation was due to the inward Al diffusion into substrate to form intermetallic phases. Porosity in the coating was also observed in the FeCrAl-Zircaloy system after HTS exposure [14].

Interactions between the coating and substrate are also observed in the different CrAl coating compositions. Fig. 4 shows the cross sectional STEM image of the 57/43 CrAl coating after 20 h 700 °C HTS exposure. A 1.5 μ m thick layer of $Zr_6(Fe,Ni)(Al,Sn)_2$ intermetallic phase was observed between the coating and Zircaloy-2 substrate. The composition of this intermetallic phase is also listed in Table 3. In addition, a much thinner 100 nm layer is observed in Fig. 4. This layer is attributed to the intermetallic phase Zr_2Al , based on GIXRD indexing shown in Fig. 1B.

A 60 nm thick alumina layer is observed on the 57/43 CrAl coating. Select area diffraction (SAD) was performed on the alumina layer using a 200 nm aperture to determine the crystal structure. This pattern is shown in Fig. 4B. The alumina is indexed as cubic γ - Al_2O_3 with a space group of $Fd-3m$. The presence of diffraction rings as opposed to diffraction spots indicate a small grain size, likely of order 10 nm. The 60 nm alumina layer with small grain size could not be effectively indexed with GIXRD (see Fig. 1B). Although SAD analysis of alumina was only performed on the 57/43 CrAl coating, we suspect γ - Al_2O_3 formation on the CrAl coatings with other compositions.

67/33 CrAl and 81/19 CrAl coatings have the lowest Al concentration in this study. Cross sectional STEM images and EDS maps of 20 h post-HTS-exposure coatings are shown in Figs. 5 and 6. Intermetallic phases are observed, although they are much thinner, compared to the layers developed in the higher Al composition coatings (42/58 CrAl and 57/43 CrAl in this study, see Figs. 3 and 4). The thickness of the intermetallic layers are not uniform.

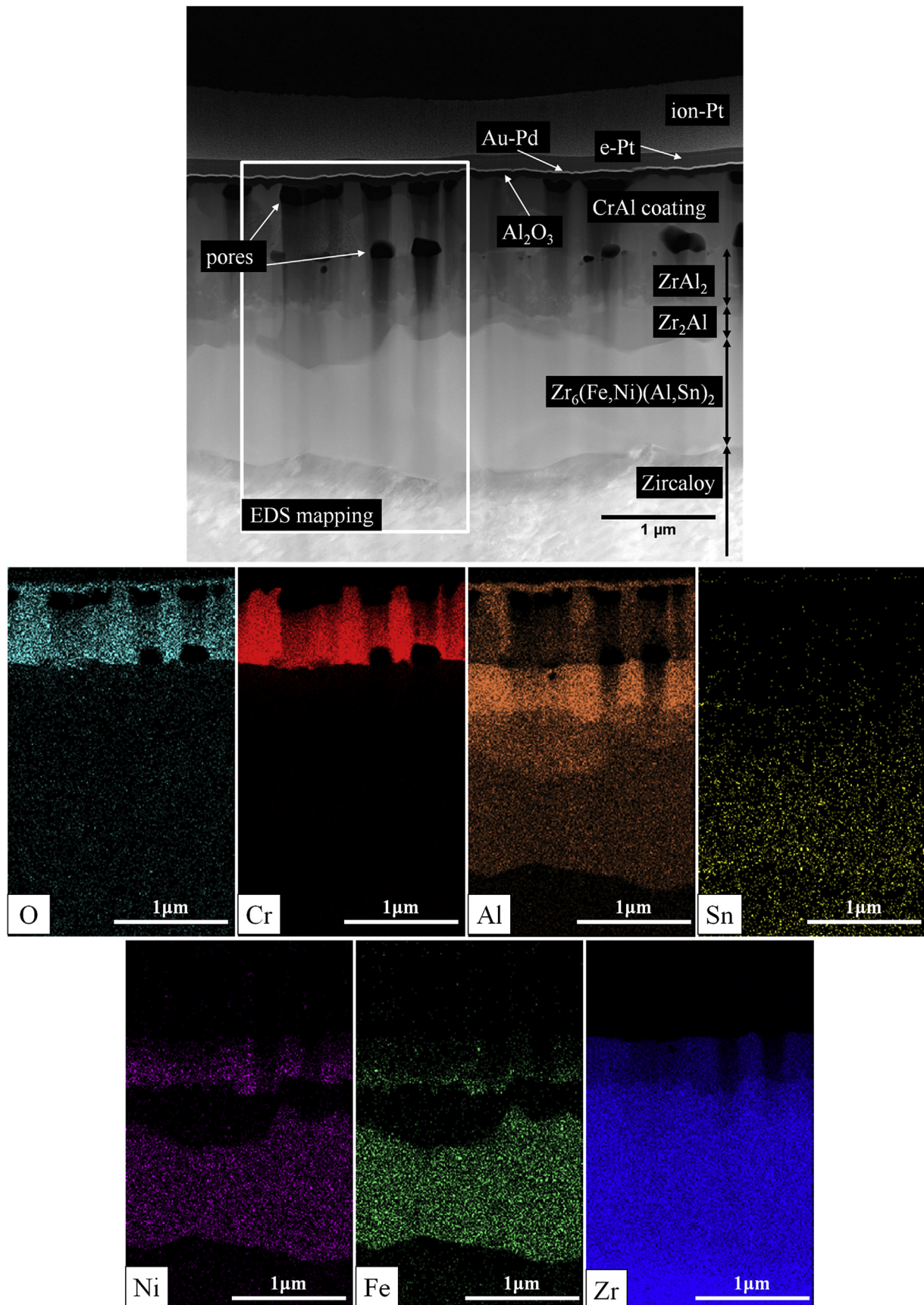


Fig. 3. Cross sectional STEM image and EDS maps of 42/58 CrAl after 10 h 700 °C HTS exposure. Layers of intermetallic phases developed between the CrAl coating and the Zircaloy matrix are labeled in the top figure. Elemental maps from EDS analysis (lower figures) demonstrate mass transport. Pores develop and are confined to the coating. Alumina formation was observed at the surface.

Composition and average thickness of the intermetallic layers of 67/33 CrAl and 81/19 CrAl coatings are included in Table 3. For 67/33 CrAl coating, $Zr_6(Fe,Ni)(Al,Sn)_2$ has two different compositions, Sn-depleted and Sn-rich. Based on the composition, both of them are $Zr_6(Fe,Ni)(Al,Sn)_2$ phase. In addition to $Zr_6(Fe,Ni)(Al,Sn)_2$ phase, a layer with the stoichiometry of $Zr(Cr,Fe,Al,Ni)_2$ is observed between the coating and the $Zr_6(Fe,Ni)(Al,Sn)_2$ layer. The total concentration of Al and Ni in $Zr(Cr,Fe,Al,Ni)_2$ is less than 8 atomic percent, while Cr concentration is as high as 43 atomic percent. Mass density difference between two intermetallic phases is not significant and the boundary between the layers is not clear from the mass-contrast STEM images (Figs. 5 and 6).

The low concentration of Al and Ni in $Zr(Cr,Fe,Al,Ni)_2$ and the similar stoichiometry of $Zr(Cr,Fe,Al,Ni)_2$ and the $Zr(Cr,Fe)_2$ SPP lead to the conclusion that Cr and Fe source in the $Zr(Cr,Fe,Al,Ni)_2$ phase is from the dissolution of $Zr(Cr,Fe)_2$ SPPs. SPP dissolution is discussed in Section 4.4. In addition, we believed Cr in the coating contributes to the formation of $Zr(Cr,Fe,Al,Ni)_2$. First, the Cr concentration in $Zr(Cr,Fe,Al,Ni)_2$ is twice the Fe concentration, while in the Zircaloy-2 $Zr(Fe,Cr)_2$ SPP, the Cr and Fe concentration is comparable [29]. Second, $Zr(Cr,Fe,Al,Ni)_2$ only forms in high Cr composition coatings, 67/33 CrAl and 81/19 CrAl. This preferential formation in high Cr composition coatings suggests Cr from the coatings contributes to the formation of the $Zr(Cr,Fe,Al,Ni)_2$ intermetallic phase. The formation of the $Zr(Cr,Fe,Al,Ni)_2$ intermetallic phase is similar to the observation of $Zr(Fe,Cr)_2$ formation in the FeCrAl/Zirconium system by Terrani et al. [25]. The $Zr(Cr,Fe,Al,Ni)_2$ intermetallic phase layer is approximately 100 nm and could not be effectively indexed with GIXRD (see Fig. 1B). We note that the intermetallic phase layers are thicker at higher Al composition (compares Figs. 3–6). This is in agreement with the GIXRD results in Fig. 1B; where stronger intermetallic peak intensity is observed for the coatings with higher Al compositions.

Both Al_2O_3 and Cr_2O_3 oxides were observed on the post-HTS-exposure 67/33 CrAl and 81/19 CrAl coatings, with Cr_2O_3 growth over Al_2O_3 . From the STEM analysis, the layer of Cr_2O_3 is thin in 67/33 CrAl coating, with a varying thickness. Only one low intensity peak of the oxide phase was observed from the XRD measurement in Fig. 1B. On the other hand, a 340 nm layer of Cr_2O_3 was observed on the post-HTS-exposure 81/19 CrAl coating, and strong intensity peaks of Cr_2O_3 were observed in the XRD result.

Plan-view SEM images of post-HTS-exposure 81/19 CrAl and pure Cr are shown in Fig. 7A and B. The Cr_2O_3 oxide has a fiber-like

morphology. Fig. 7C is the plan view SEM image of the post-HTS-exposure 57/43 CrAl. The plan view image does not show the microstructure of alumina because of the fine grains and thin layer thickness. However, the porosity confined to the coating is evident.

4. Discussion

4.1. Oxidation weight gain of CrAl coatings at 700 °C steam environment

Significant oxidation of Zircaloy and hydrogen ingress are expected to occur at the uncoated edges of coated samples. However, weight gain due to oxidation is an important quantity for accident tolerant coating evaluation. We therefore base the oxidation weight gain on the cross sectional STEM analysis of the chromia and alumina thickness. On the other hands, the uncoated Zircaloy-2 does not have edge effects, and therefore, the weight gain of uncoated Zircaloy-2 is based on the thermogravimetric weight gain measurement during the HTS exposure. Weight gain data are shown in Fig. 8. The largest weight gain of coated Zircaloy-2 (0.67 g/m²) was observed for the 81/19 CrAl coating after 20 h HTS exposure, which corresponds to a 340 nm layer of Cr_2O_3 and a 60 nm layer of Al_2O_3 , acknowledging that variation exists regarding the alumina thickness, as shown in Fig. 6. A 60 nm alumina layer is observed for the 42/58 CrAl and 57/43 CrAl coatings after 20 h HTS exposure (see Fig. 4 for 57/43 CrAl), which corresponds to a weight gain of 0.11 g/m². As expected, alumina provides better protection than chromia with respect to the oxidation weight gain. For reference, a weight gain of 231 g/m² was observed for uncoated Zircaloy-2 after 20 h exposure to 700 °C HTS. Weight gain of 10 h exposed 42/58 CrAl coating is also included in Fig. 8. The reduced oxidation kinetics in prolong exposure is demonstrated by comparing 10 h and 20 h exposure for the 42/58 CrAl coating.

4.2. Protective elements consumption by oxide and substrate

The formation of Al_2O_3 or Cr_2O_3 surface oxides and intermetallic phase layers were observed for the post-HTS-exposure CrAl coatings. Intermetallic phase formation reduces the inventory of oxide-forming elements (Al and Cr) available in the coatings. This effect will be more severe for thin coatings. The consumptions of Al and Cr to form surface oxide or to form intermetallic phases can be

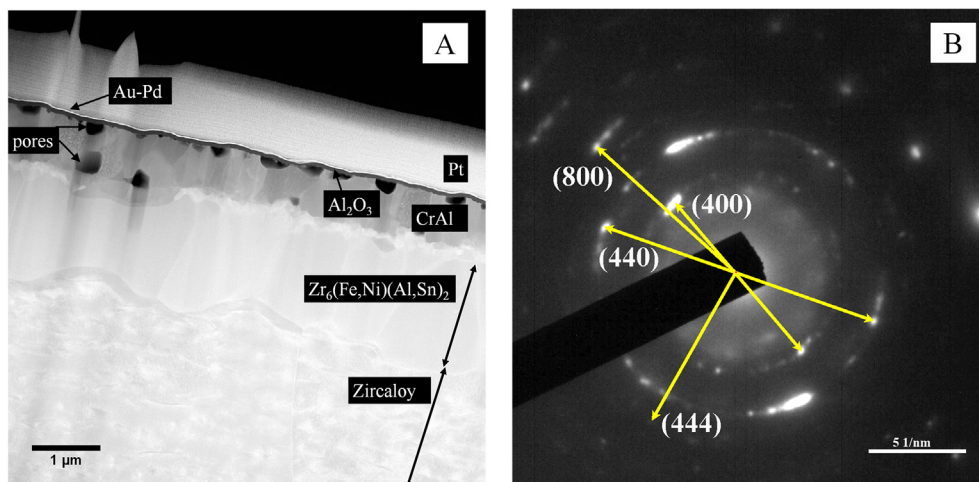


Fig. 4. STEM cross sectional image of 57/43 CrAl coating after 20 h 700 °C HTS exposure (left figure). Pores are observed confined to the coating. A 60 nm layer of alumina developed, and it is indexed as γ - Al_2O_3 by SAD. The SAD pattern of γ - Al_2O_3 is shown (right figure).

estimated by,

$$W = \sum_i \rho_i t_i W_{f,i} \quad (2)$$

where, ρ_i is the density of the i th layer, t_i is the thickness of the i th layer, $W_{f,i}$ is the weight fraction of the Al or Cr in the i th layer, and W is the total weight consumption of the Al or Cr per unit area.

The density of $\text{Zr}(\text{Cr,Fe,Al,Ni})_2$ is required to calculate the amount of Cr consumption to the intermetallic phases for 67/33 CrAl and 81/19 CrAl coatings. However, the layer of $\text{Zr}(\text{Cr,Fe,Al,Ni})_2$ is too thin to be indexed in the GIXRD measurement; the crystal lattice structure and therefore the density are unknown. We

assume the $\text{Zr}(\text{Cr,Fe,Al,Ni})_2$ intermetallic phase has the same density of the $\text{Zr}(\text{Cr,Fe})_2$ SPP (7.124 g/cm^3). We believe this is reasonable given the low concentration of Al and Ni in $\text{Zr}(\text{Cr,Fe,Al,Ni})_2$ and similar stoichiometry.

The formation of $\text{Zr}(\text{Cr,Fe,Al,Ni})_2$ has Cr and Fe contribution from the dissolution of the $\text{Zr}(\text{Cr,Fe})_2$ SPPs. Therefore, the amount of Cr from the $\text{Zr}(\text{Cr,Fe})_2$ SPP contribution needs to be subtracted from the total amount of Cr in $\text{Zr}(\text{Cr,Fe,Al,Ni})_2$ to estimate the loss from the coating. The weight fraction of Cr in the $\text{Zr}(\text{Cr,Fe,Al,Ni})_2$ intermetallic phase layer from the $\text{Zr}(\text{Cr,Fe})_2$ SPP contribution is assumed to be equivalent to the weight fraction of Fe in $\text{Zr}(\text{Cr,Fe,Al,Ni})_2$ due to the similar concentration of Cr and Fe in $\text{Zr}(\text{Cr,Fe})_2$ [29]. Therefore, we can then estimate the consumption of

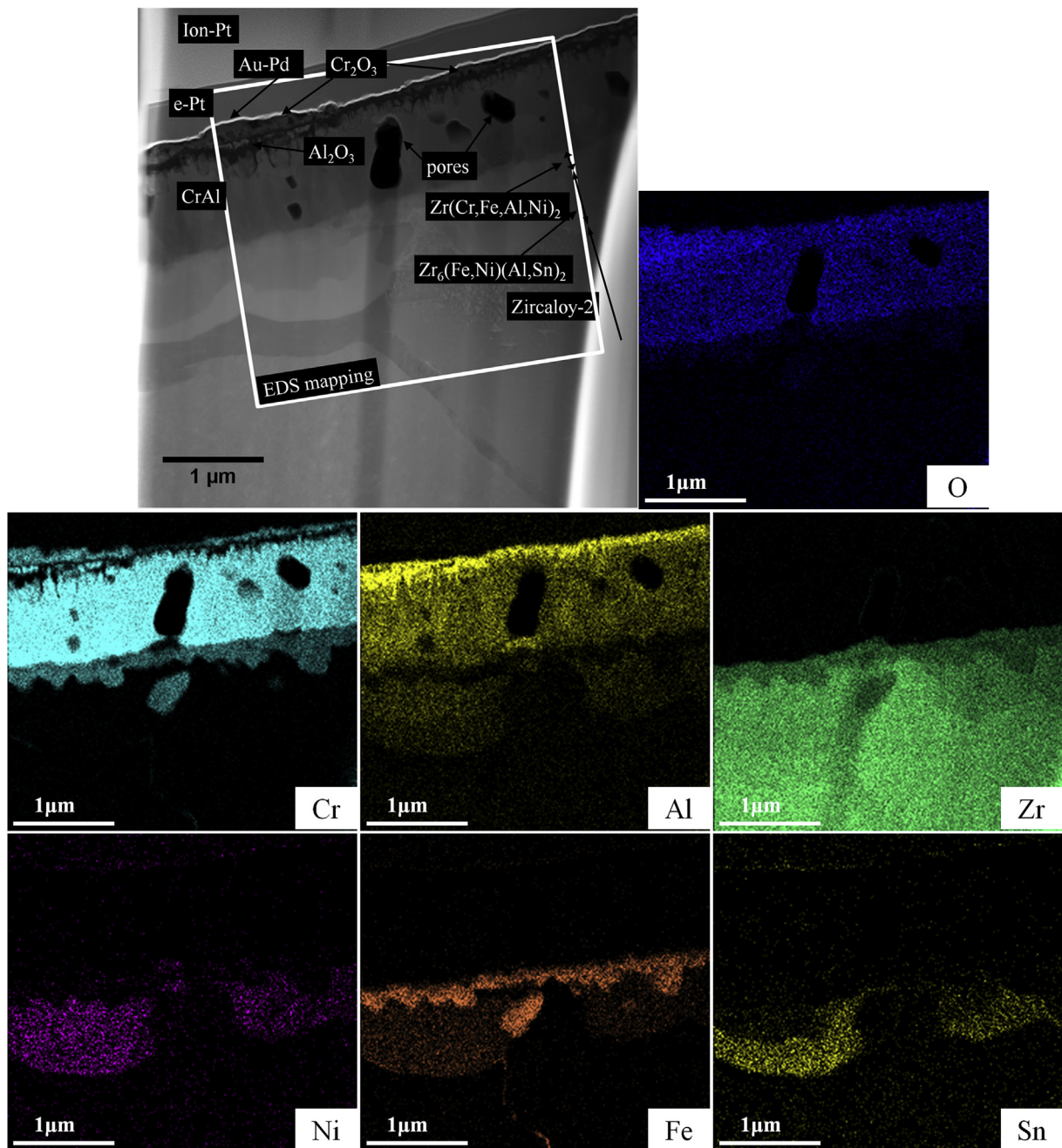


Fig. 5. STEM cross sectional image and EDS maps of 67/33 CrAl coating after 20 h 700 °C HTS exposure. Both Cr_2O_3 and Al_2O_3 oxides form. Intermetallic layers of $\text{Zr}_6(\text{Fe,Ni})(\text{Al,Sn})_2$ and $\text{Zr}(\text{Cr,Fe,Al,Ni})_2$ are observed.

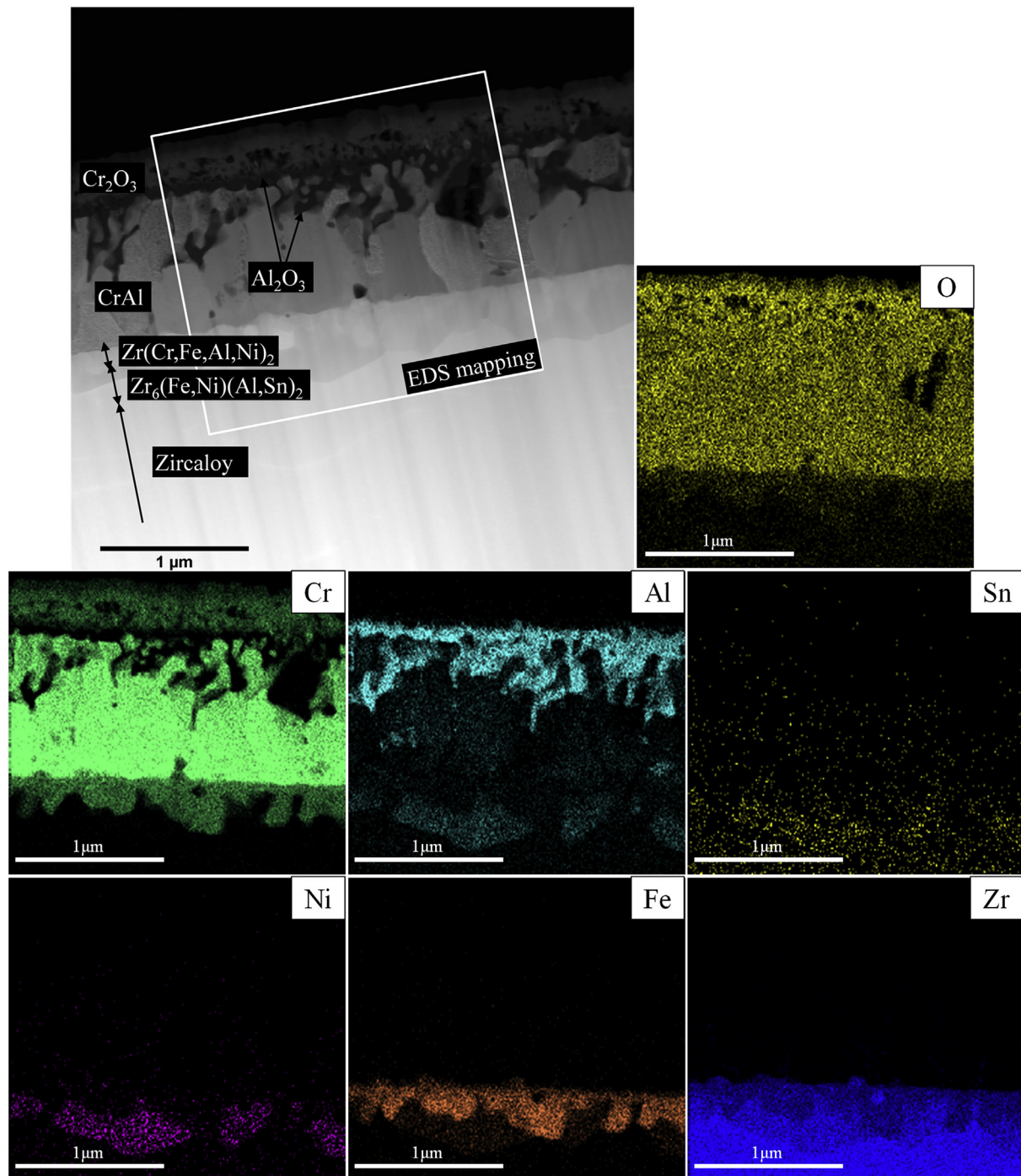


Fig. 6. STEM cross sectional image and EDS maps of 81/19 CrAl coating after 20 h 700 °C HTS exposure. Al_2O_3 and thick layer of Cr_2O_3 are evident. Intermetallic layers of $\text{Zr}(\text{Cr,Fe,Al,Ni})_2$ and $\text{Zr}_6(\text{Fe,Ni})(\text{Al,Sn})_2$ are observed. The intermetallic phase layers are thinner than the higher Al composition coatings.

Cr from the coating to intermetallic phases as,

$$W = \rho t (W_{f,\text{Cr}} - W_{f,\text{Fe}}) \quad (3)$$

where $W_{f,\text{Cr}}$ is the weight fraction of Cr in the $\text{Zr}(\text{Cr,Fe,Al,Ni})_2$ intermetallic phase layer and $W_{f,\text{Fe}}$ is the weight fraction of Fe in the $\text{Zr}(\text{Cr,Fe,Al,Ni})_2$ intermetallic phase layer. This analysis is applicable to the 67/33 CrAl and 81/19 CrAl coatings to calculate the Cr consumption to intermetallic phases.

Table 4 summarizes the amount of Al and Cr consumption to the

surface oxide formation and to the intermetallic phase layer formation. For HTS exposure of 42/58 CrAl (10 h) and 57/43 CrAl (20 h), thin layers of alumina formed and the amount of Al consumption to the oxide is very low, 0.1 and 0.12 g/m², respectively. On the other hand, significant Al consumption to intermetallic phase layer formation is estimated to be 1.1 g/m² and 0.47 g/m² for 42/58 CrAl and 57/43 CrAl coatings respectively. A total of 67% of the Al inventory in the initial coating was consumed by the 10 h HTS exposure for 42/58 CrAl coating. Aluminum consumption of the intermetallic phase formation was reduced for 57/43 CrAl

Table 3

Composition (atomic percent) and thickness of intermetallic layers of post-HTS-exposure CrAl coatings.

Coating	Intermetallic phase	Al	Cr	Fe	Ni	Sn	Zr	Thickness [nm]
42/58 CrAl	ZrAl ₂	51	4.7	4	6	—	34.3	400
	Zr ₂ Al	32.5	—	—	—	—	67.5	300
	Zr ₆ (Fe,Ni) (Al,Sn) ₂	17.7	—	7.2	6.5	3.4	65.2	1100
57/43 CrAl	Zr ₆ (Fe,Ni) (Al,Sn) ₂	15.9	—	7.0	7.3	2.5	67.3	1400
67/33 CrAl	Zr(Cr,Fe,Al,Ni) ₂	5.7	42.3	17	1.3	—	33.7	150
	Zr ₆ (Fe,Ni) (Al,Sn) ₂ -Sn depleted	17.1	1.5	6.5	6.5	3.3	65.1	250
	Zr ₆ (Fe,Ni) (Al,Sn) ₂ -Sn rich	10.2	1.6	7.1	5.6	11.7	63.8	150
81/19 CrAl	Zr(Cr,Fe,Al,Ni) ₂	4.4	43.4	16.2	1.1	—	34.9	200
	Zr ₆ (Fe,Ni) (Al,Sn) ₂	17.6	1.4	6.3	6.4	3.8	64.5	100

coating to only 0.47 g/m². A total of 37.6% Al consumption is estimated for 57/43 CrAl coating after 20 h. Both 42/58 CrAl and 57/43 CrAl coatings have more Al consumption of the intermetallic layer phase than to the surface oxides. This is in contrast to higher Cr composition coatings (67/33 CrAl and 81/19 CrAl) that exhibit greater Al and Cr consumption to surface oxides. Significant Al consumption to Zr substrate was also observed in other coatings containing Al [30,31]. A barrier layer is proposed to retard the Al diffusion, such as TiN [30] and Cr.

4.3. CrAl coating lattice structure and microstructural change

Post-HTS-exposure, 42/58 CrAl sample exhibited different coating lattice structure and microstructure from the as-deposited coating. The as-deposited 42/58 CrAl coating was indexed as the

rhombohedral Al₈Cr₅ (R3m) structure in Fig. 1A. The alumina growth and intermetallic formation consume the Al inventory in the coating. As a result, the coating structure transforms to the tetragonal AlCr₂ structure (P4/mmm). The transformation is evident by the presence of the (200) peak of the tetragonal AlCr₂ in GIXRD (see Fig. 1B). We believe the elevated temperature associated with 700 °C HTS facilitated the phase transformation. For post-HTS-exposure 81/19 CrAl, the peak position of the coating is at the corrected cubic Cr peak position (see Fig. 1B), as opposed to the shifted diffraction peak position for the as-deposited coating (see Fig. 1A). The reduced Al composition in the coating after steam exposure and the grain relaxation at 700 °C could lead to corrected coating peak position.

In addition, the microstructure of the 42/58 CrAl changed after the HTS exposure. The as-deposited coating demonstrates columnar grains structure (see Fig. 2A), which is dependent on the coating deposition condition [32]. The coating transformed to an equiaxed grain structure after the HTS exposure (see Fig. 3). We believe that the coating structure transformation occurs to minimize the grain boundary area, which is enhanced by the elevated temperature associated with the HTS exposure. Furthermore, aluminum consumption lead to the film thickness reduction. The 42/58 CrAl coating thickness reduced to 700 nm after 10 h 700 °C HTS exposure (see Fig. 3) from the 1 μm as-deposited thickness (see Fig. 2A).

4.4. Dissolution of second phase particles

Second phase particle dissolution in favor of intermetallic phase formation is driven by the presence of Al and Cr in the coatings. The elevated temperature associated with the HTS exposure facilitates the required mass transport and may alter the phase stability. Two

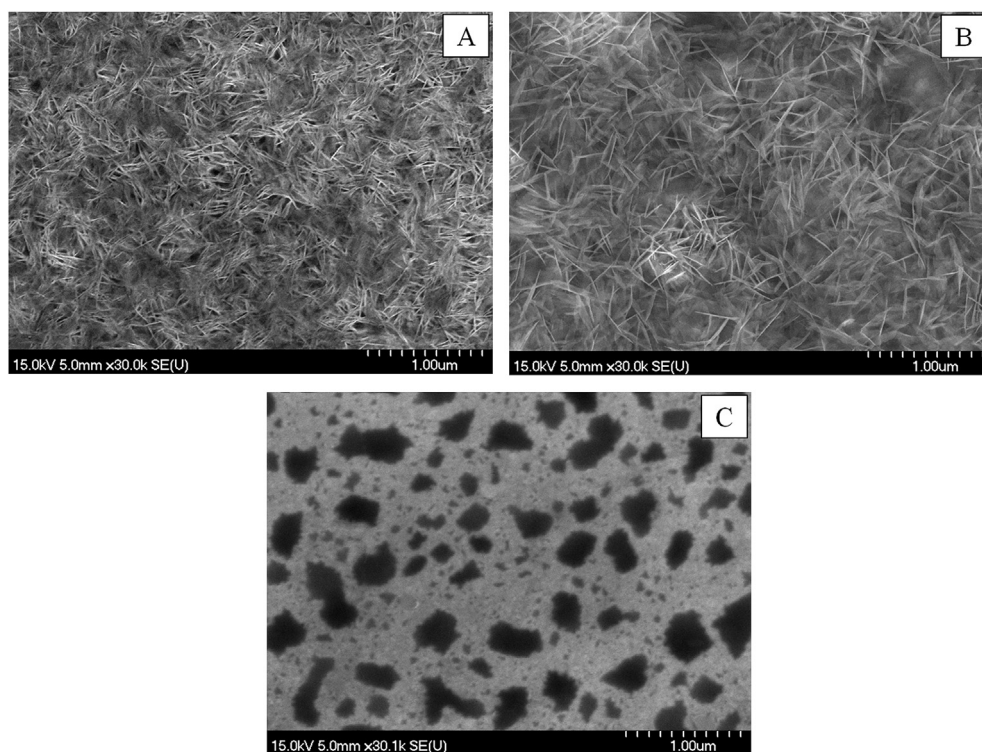


Fig. 7. Plan view SEM images of CrAl and Cr coatings after 20 h 700 °C HTS exposure. (A) 81/19 CrAl coatings; (B) Cr coatings; (C) 57/43 CrAl coatings. Cr₂O₃ developed on the 81/19 CrAl and Cr coating, and fiber-like structure of Cr₂O₃ was observed on the surface. γ-alumina developed on the 57/43 CrAl coating. The grains and the thickness of the alumina are small, as shown in the STEM image in Fig. 4. The plan view image of post-HTS-exposure 57/43 CrAl coatings in (C) does not demonstrate Al₂O₃ microstructure. Porosity in the 57/43 CrAl coating is observed.

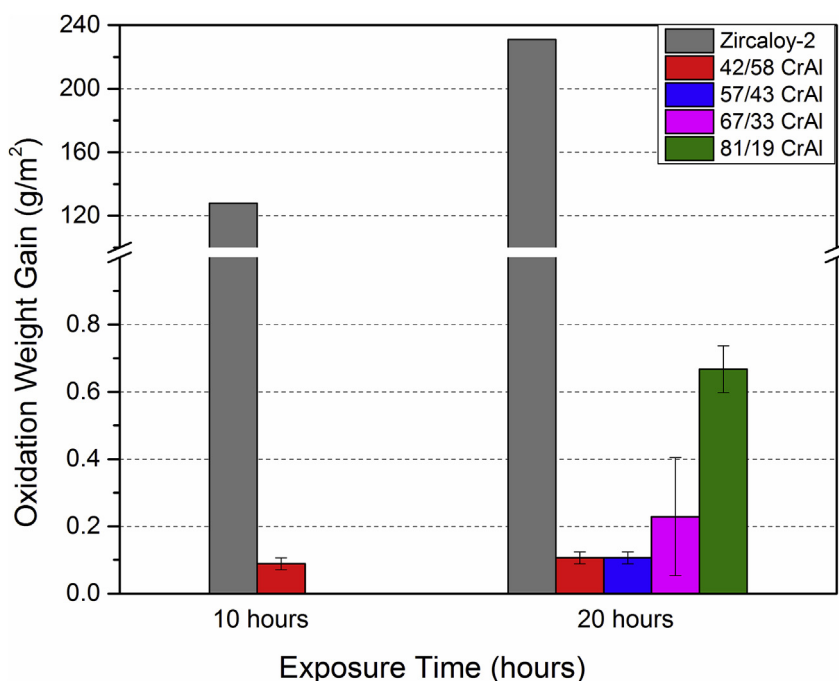


Fig. 8. Calculated oxidation weight gain at 700 °C HTS exposure for CrAl coatings with different compositions based on cross section STEM analysis. Largest weight gain of coated Zircaloy at 20 h exposure was observed on the highest Cr composition coating, 81/19 CrAl, where a 340 nm layer of Cr_2O_3 formed. The lowest weight gain was observed on the highest Al composition coatings (42/58 CrAl and 57/43 CrAl), with a 60 nm layer of Al_2O_3 . Weight gain of 42/58 CrAl after 10 h exposure is included. Error bars are included to describe the non-uniformity of oxide thickness from STEM analysis. For reference, a weight gain of 128 g/m² was observed for uncoated Zircaloy-2 after 10 h 700 °C HTS exposure, and 231 g/m² after 20 h 700 °C HTS exposure. The weight gain for the uncoated Zircaloy-2 is based on the TGA weight gain measurement during the exposure.

Table 4

Element transport to the surface oxide and intermetallic phase formation for CrAl coating samples.

	42/58 CrAl	57/43 CrAl	67/33 CrAl	81/19 CrAl
Element inventory in the as-deposited coatings (g/m ²)	Cr 2.49	4.02	4.45	6.42
Consumption to surface oxide formation (g/m ²)	Al 1.79	1.57	1.14	0.78
Consumption to intermetallic phases formation (g/m ²)	Cr 0	0	0.3	1.22
Ratio of the consumption amount versus the original element inventory in the coatings	Al 0.1	0.12	0.1	0.12
	Cr 0.08	0	0.24	0.31
	Al 1.10	0.47	0.15	0.06
	Cr 3.2%	0%	12.1%	23.8%
	Al 67.0%	37.6%	21.9%	23.1%

intermetallic phase layers $[\text{ZrAl}_2 \text{ and } \text{Zr}_6(\text{Fe,Ni}) (\text{Al,Sn})_2]$ containing Ni for the 42/58 CrAl coating were observed. Nickel has limited solubility in α -Zr phase [33]. Kruger et al. measured a Ni solubility of 0.0086% by weight in beta-quenched Zircaloy-2 matrix [34]. The amount of dissolved Ni in Zircaloy-2 is less than the amount of Ni that formed intermetallic phases (see Appendix). This indicates the dissolution of SPPs during the HTS exposure must occur to provide Ni for the formation of the intermetallic phases. The dissolution of SPPs also occurs in other post-HTS-exposure CrAl coatings.

The intermetallic phase formation involving Fe, Cr and Ni is facilitated by the rapid diffusion of these elements in α -Zr phase [35–37]. The average diffusivity of Fe, Cr and Ni in α -Zr at 700 °C is approximately $3.6 \times 10^{-11} \text{ m}^2/\text{s}$, $1.0 \times 10^{-13} \text{ m}^2/\text{s}$ and $7 \times 10^{-11} \text{ m}^2/\text{s}$ respectively [36]. These lead to diffusion distances of 3200um, 170um, and 4500um for 20 h at 700 °C for Fe, Cr and Ni respectively. Alloying elements in Zr affect these diffusivities. For example, the diffusivities of Fe and Ni in Zircaloy-2 at 700 °C decrease to $2.55 \times 10^{-12} \text{ m}^2/\text{s}$ [36] and $3.27 \times 10^{-12} \text{ m}^2/\text{s}$ [38] by extrapolation from Hood's measurement. The diffusion distances of Fe and Ni in

Zircaloy at 700 °C for 20 h is 860um and 970um respectively. Such rapid diffusion in Zircaloy-2 facilitates the intermetallic phase formation involving Fe and Ni.

5. Conclusions

Pure Cr and CrAl coatings with different compositions (Cr/Al atomic percent of 100/00, 42/58, 57/43, 67/33, and 81/19) deposited on Zircaloy-2 have been studied with respect to oxidation performance in 700 °C HTS. Alumina formed on the surface of high Al composition coatings (42/58 CrAl and 57/43 CrAl) and it was indexed as cubic γ - Al_2O_3 in TEM analysis. For high Cr composition coatings (67/33 CrAl and 81/19 CrAl), both Cr_2O_3 and Al_2O_3 formation was observed. Weight gain estimates from STEM analysis demonstrate that the coatings with higher Al composition have lower oxidation kinetics during 700 °C HTS exposure.

Intermetallic phase layers were observed to form during HTS exposure. This is attributed to an interaction between the coatings and the Zircaloy-2 substrate. The compositions and the thickness of the intermetallic phases were dependent on the coating composition. A layer of tetragonal $\text{Zr}_6(\text{Fe,Ni}) (\text{Al,Sn})_2$ was observed for all post-HTS-exposure CrAl coatings. Binary intermetallic phases ZrAl_2 and Zr_2Al were observed in the coatings with high Al composition (42/58 CrAl and 57/43 CrAl). For high Cr composition coatings (67/33 CrAl and 81/19 CrAl), both the $\text{Zr}(\text{Cr,Fe,Al,Ni})_2$ and $\text{Zr}_6(\text{Fe,Ni}) (\text{Al,Sn})_2$ intermetallic phases were observed. Estimates of Ni consumption indicate SPP dissolution must occur during the HTS exposure.

Aluminum and Cr consumption to form surfaces oxide and intermetallic phase layers during HTS exposure were estimated. Aluminum consumption to the intermetallic phase formation is more significant than to the oxide formation for high Al composition coatings (42/58 CrAl and 57/43 CrAl). For high Cr composition coatings (67/33 CrAl and 81/19 CrAl), the consumption of Cr to

oxide formation become larger. All CrAl and Cr coatings with the thickness of 1 μm reduce Zr oxidation in 700 °C HTS for 20 h. Thicker coatings will results in lower fractional Al and Cr consumption and longer protection times.

Acknowledgments

This work was supported by the US Department of Energy Nuclear Energy University Programs Integrated Research Project under contract number IRP-12-4728. In addition, the microanalysis was performed mainly in the Frederick Seitz Materials Research Laboratory Central Facilities, University of Illinois, which are partially supported by the U.S. Department of Energy under Grants DE-FG02-07ER46453 and DE-FG02-07ER46471.

Appendix

Calculations were performed to estimate the amount of dissolved Ni in Zircaloy-2 and the amount of Ni that form intermetallic phases with the coating based on the cross sectional STEM/EDS analysis. Two intermetallic phases that contain Ni for the 42/58 CrAl coating are ZrAl_2 and $\text{Zr}_6(\text{Fe,Ni})(\text{Al,Sn})_2$, whose thickness are 0.4 μm and 1.1 μm respectively (see Table 3). The concentration of Ni in each layer are 6.6 wt% and 5 wt%, and the density of ZrAl_2 and $\text{Zr}_6(\text{Fe,Ni})(\text{Al,Sn})_2$ are 4.567 g/cm³ and 5.976 g/cm³ respectively. The total amount of Ni in the intermetallic phases is calculated using Eqn. (2) as following shows. A factor of two is included in the calculation, as the Zircaloy-2 coupon is double side coated, and the intermetallic phases are developed on both sides.

$$(4.567 \text{ g/cm}^3 \times 0.066 \times 0.4\mu\text{m} + 5.976 \text{ g/cm}^3 \times 0.05 \times 1.1\mu\text{m}) \times 2 = 0.9 \text{ g/m}^2$$

Typical composition of Zircaloy-2 is provided in Table 5. Zircaloy-2 sheet contains 0.05 wt% Ni. However, only a fraction of 0.0086% by weight of Ni solubility in beta-quenched Zircaloy-2 matrix was reported by Kruger et al. [34]. Hence, the area density of Ni in Zircaloy-2 is calculated as,

$$6.55 \text{ g/cm}^3 \times 1 \text{ mm} \times 0.0086 \% = 0.56 \text{ g/m}^2$$

where 1 mm is the thickness of the Zircaloy coupon. The amount of dissolved Ni in as-received Zircaloy-2 is less than the amount of Ni that formed intermetallic phases. Therefore, dissolution of $\text{Zr}_2(\text{Fe,Ni})$ SPPs must occur to provide Ni for the intermetallic phases formation.

Table 5

Typical composition (weight percent) of Zircaloy-2.

Tin	Iron	Chromium	Nickel	Zirconium
1.5	0.15	0.10	0.05	Balance

References

- [1] Z. Duan, H. Yang, Y. Satoh, K. Murakami, S. Kano, Z. Zhao, J. Shen, H. Abe, Current status of materials development of nuclear fuel cladding tubes for light water reactors, Nucl. Eng. Des. 316 (2017) 131–150.
- [2] S.J. Zinkle, K.A. Terrani, J.C. Gehin, L.J. Ott, L.L. Snead, Accident tolerant fuels for LWRs: a perspective, J. Nucl. Mater. 448 (1) (2014) 374–379.
- [3] T. Alam, M.K. Khan, M. Pathak, K. Ravi, R. Singh, S.K. Gupta, A review on the clad failure studies, Nucl. Eng. Des. 241 (9) (2011) 3658–3677.
- [4] M. Steinbrück, M. Böttcher, Air oxidation of Zircaloy-4, M5® and ZIRLO™ cladding alloys at high temperatures, J. Nucl. Mater. 414 (2) (2011) 276–285.
- [5] K.A. Terrani, S.J. Zinkle, L.L. Snead, Advanced oxidation-resistant iron-based alloys for LWR fuel cladding, J. Nucl. Mater. 448 (1) (2014) 420–435.
- [6] B.A. Pint, K.A. Terrani, M.P. Brady, T. Cheng, J.R. Keiser, High temperature oxidation of fuel cladding candidate materials in steam–hydrogen environments, J. Nucl. Mater. 440 (1) (2013) 420–427.
- [7] C. Badini, F. Laurella, Oxidation of FeCrAl alloy: influence of temperature and atmosphere on scale growth rate and mechanism, Surf. coatings Technol. 135 (2) (2001) 291–298.
- [8] Y. Yan, J.R. Keiser, K.A. Terrani, G.L. Bell, L.L. Snead, Post-quench ductility evaluation of Zircaloy-4 and select iron alloys under design basis and extended LOCA conditions, J. Nucl. Mater. 448 (1) (2014) 436–440.
- [9] K. Yueh, K.A. Terrani, Silicon carbide composite for light water reactor fuel assembly applications, J. Nucl. Mater. 448 (1) (2014) 380–388.
- [10] Y. Lee, T.J. McKrell, C. Yue, M.S. Kazimi, Safety assessment of SiC cladding oxidation under loss-of-coolant accident conditions in light water reactors, Nucl. Technol. 183 (2) (2013) 210–227.
- [11] L.L. Snead, T. Nozawa, Y. Katoh, T.-S. Byun, S. Kondo, D.A. Petti, Handbook of SiC properties for fuel performance modeling, J. Nucl. Mater. 371 (1) (2007) 329–377.
- [12] C.P. Deck, G.M. Jacobsen, J. Sheeder, O. Gutierrez, J. Zhang, J. Stone, H.E. Khalifa, C.A. Back, Characterization of SiC–SiC composites for accident tolerant fuel cladding, J. Nucl. Mater. 466 (2015) 667–681.
- [13] K.A. Terrani, B.A. Pint, C.M. Parish, C.M. Silva, L.L. Snead, Y. Katoh, Silicon carbide oxidation in steam up to 2 MPa, J. Am. Ceram. Soc. 97 (8) (2014) 2331–2352.
- [14] W. Zhong, P.A. Mouche, X. Han, B.J. Heuser, K.K. Mandapaka, G.S. Was, Performance of iron–chromium–aluminum alloy surface coatings on Zircaloy 2 under high-temperature steam and normal BWR operating conditions, J. Nucl. Mater. 470 (2016) 327–338.
- [15] D. Park, P.A. Mouche, W. Zhong, K.K. Mandapaka, and G.S. Was, B.J. Heuser. TEM/STEM study of Zircaloy-2 with protective FeCrAl layers under simulated BWR environment and high-temperature steam exposure, J. Nucl. Mater. under Rev.
- [16] J.-H. Chun, S.-W. Lim, B.-D. Chung, W.-J. Lee, Safety evaluation of accident-tolerant FCM fueled core with SiC-coated zircalloy cladding for design-basis accidents and beyond DBAs, Nucl. Eng. Des. 289 (2015) 287–295.
- [17] T. Usui, A. Sawada, M. Amaya, A. Suzuki, T. Chikada, T. Terai, SiC coating as hydrogen permeation reduction and oxidation resistance for nuclear fuel cladding, J. Nucl. Sci. Technol. 52 (10) (2015) 1318–1322.
- [18] B.R. Maier, B.L. Garcia-Diaz, B. Hauch, L.C. Olson, R.L. Sindelar, K. Sridharan, Cold spray deposition of Ti 2 AlC coatings for improved nuclear fuel cladding, J. Nucl. Mater. 466 (2015) 712–717.
- [19] E. Alat, A.T. Motta, R.J. Comstock, J.M. Partezana, D.E. Wolfe, Multilayer (TiN, TiAlN) ceramic coatings for nuclear fuel cladding, J. Nucl. Mater. 478 (2016) 236–244.
- [20] J.C. Brachet, M.L. Saux, M.L. Flem, S. Urvoay, E. Rouesne, On-going Studies at CEA on Chromium Coated Zirconium Based Nuclear Fuel Claddings for Enhanced Accident Tolerant LWRs Fuel, TopFuel 2015, 2015. Zurich, Switzerland.
- [21] D.J. Park, H.G. Kim, Y.I. Jung, J.H. Park, J.H. Yang, Y.H. Koo, Behavior of an improved Zr fuel cladding with oxidation resistant coating under loss-of-coolant accident conditions, J. Nucl. Mater. 482 (2016) 75–82.
- [22] J.H. Park, H.G. Kim, J.Y. Park, Y.I. Jung, D.J. Park, Y.H. Koo, High temperature steam-oxidation behavior of arc ion plated Cr coatings for accident tolerant fuel claddings, Surf. Coatings Technol. 280 (2015) 256–259.
- [23] M. Steinbrück, Prototypical experiments relating to air oxidation of Zircaloy-4 at high temperatures, J. Nucl. Mater. 392 (3) (2009) 531–544.
- [24] K. Barrett, S. Bragg-Sitton, D. Galicki, Advanced LWR Nuclear Fuel Cladding System Development Trade-off Study, INL/EXT-12–27090, 2012.
- [25] K.A. Terrani, C.M. Parish, D. Shin, B.A. Pint, Protection of zirconium by alumina and chromia-forming iron alloys under high-temperature steam exposure, J. Nucl. Mater. 438 (1) (2013) 64–71.
- [26] M.M. Strehle, B.J. Heuser, M.S. Elbakshswan, X. Han, D.J. Gennardo, H.K. Pappas, H. Ju, Thin Solid Films 520 (2012) 5616.
- [27] J.A. Thornton, D.W. Hoffman, Stress-related effects in thin films, Thin solid films 171 (1) (1989) 5–31.
- [28] J.H. Hubbell, S.M. Seltzer, Tables of X-ray Mass Attenuation Coefficients and Mass Energy-absorption Coefficients 1 KeV to 20 MeV for Elements Z = 1 to 92 and 48 Additional Substances of Dosimetric Interest. No. PB–95–220539/XAB; NISTIR–5632. National Inst. Of Standards and Technology-PL, Ionizing Radiation Div., Gaithersburg, MD (United States), 1995.
- [29] X. Meng, D.O. Northwood, Second phase particles in Zircaloy-2, J. Nucl. Mater. 168 (1–2) (1989) 125–136.
- [30] E. Alat, A.T. Motta, R.J. Comstock, J.M. Partezana, D.E. Wolfe, Multilayer (TiN, TiAlN) ceramic coatings for nuclear fuel cladding, J. Nucl. Mater. 478 (2016) 236–244.
- [31] D.J. Tallman, J. Yang, L. Pan, B. Anasori, M.W. Barsoum, Reactivity of Zircaloy-4 with Ti 3 SiC 2 and Ti 2 AlC in the 1100–1300° C temperature range, J. Nucl. Mater. 460 (2015) 122–129.
- [32] J.A. Thornton, Influence of apparatus geometry and deposition conditions on the structure and topography of thick sputtered coatings, J. Vac. Sci. Technol. 11 (4) (1974) 666–670.
- [33] A. Yilmazbayhan, O. Delaire, A.T. Motta, R.C. Birtcher, J.M. Maser, B. Lai, Determination of the alloying content in the matrix of Zr alloys using synchrotron radiation microprobe X-ray fluorescence, J. Nucl. Mater. 321 (2) (2003) 221–232.

- [34] R.M. Kruger, R.B. Adamson, S.S. Brenner, Effects of microchemistry and precipitate size on nodular corrosion resistance of Zircaloy-2, *J. Nucl. Mater.* 189 (2) (1992) 193–200.
- [35] G.M. Hood, R.J. Schultz, Ultra-fast solute diffusion in α -Ti and α -Zr, *Philos. Mag.* 26.2 (1972) 329–336.
- [36] G.M. Hood, R.J. Schultz, Diffusion of 3D transition elements in α -Zr and zirconium alloys, in: *Zirconium in the Nuclear Industry: Eighth International Symposium*. ASTM International, 1989.
- [37] H. Nakajima, G.M. Hood, R.J. Schultz, Diffusion of ^{59}Fe in single-crystal α -Zr, *Philos. Mag. B* 58 (3) (1988) 319–337.
- [38] G.M. Hood, R.J. Schultz, *Ni Diffusion in Zr and Zr Alloys*. Materials Science Forum, 15, Trans Tech Publications, 1987.